Supplementary information

Bypassing thermodynamic immiscibility via electrochemical kinetic atom trapping

Min-Ho Kim[1,2,†,*], Jin Koo Kim[1,3,†], Kaiyan Liang[1,†], Hayoung Park[1,4], Tian-Yu Wang[1], Huida Lyu[1], Kaixi Chen[1], Dingyi Zhao[1], Jung Tae Kim[1], Jinyoung Kim[1], Yuzhang Li[1,*]

[1]Department of Chemical and Biomolecular Engineering, University of California, Los Angeles (UCLA); Los Angeles, CA 90095, USA

[2]Present address: Department of Energy Engineering, Korea Institute of Energy Technology; Naju 58330, Republic of Korea

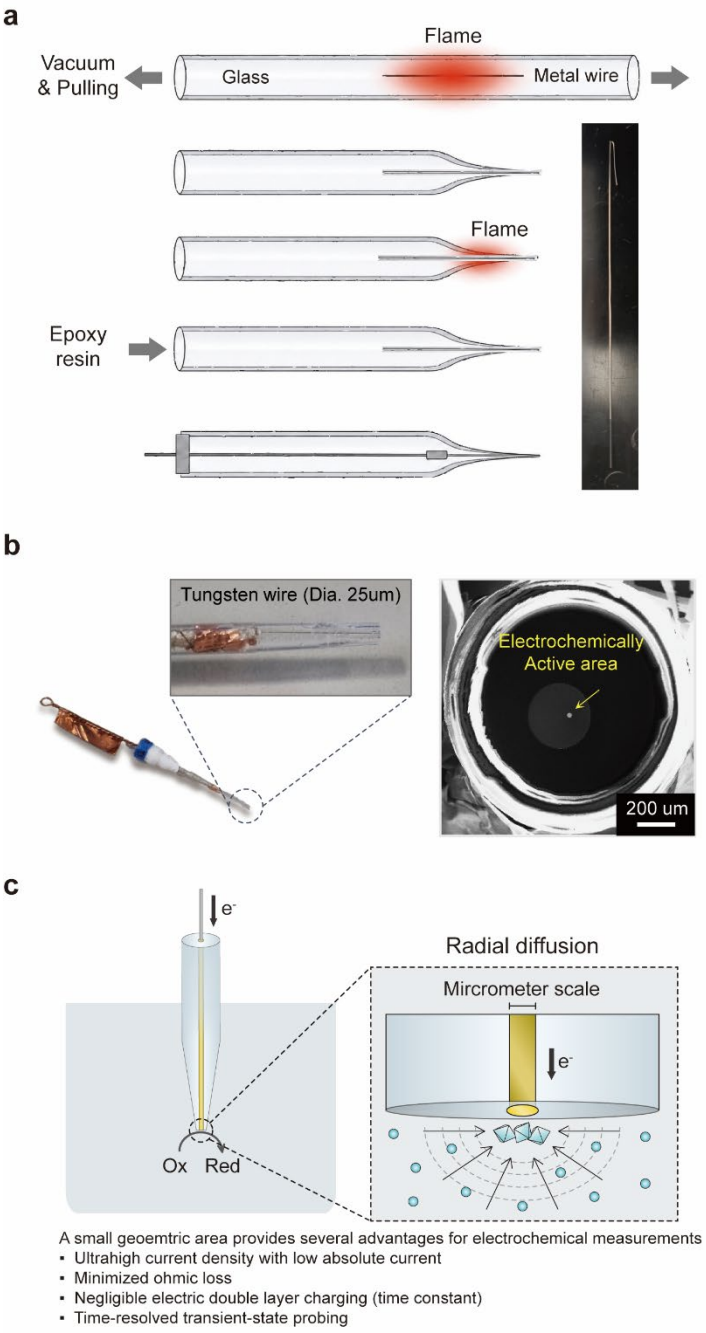
[3]Present address: Advanced Cell Research Center, LG Energy Solution; Daejeon 34122, Republic of Korea

[4]Present address: Department of Chemical Engineering and Materials Science, Ewha Woman's University; Seoul 03760, Republic of Korea

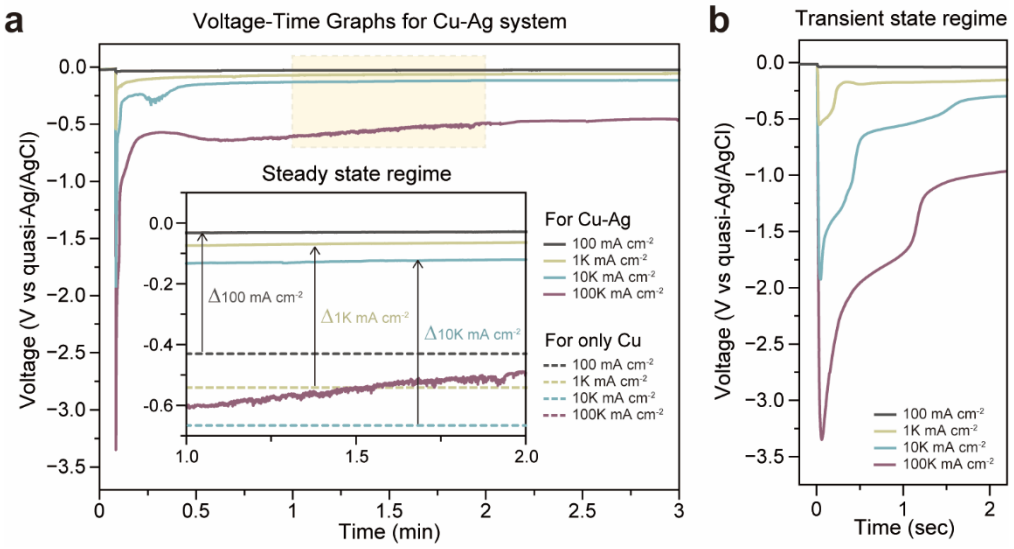
*Corresponding authors. Email: minhokim@kentech.ac.kr, yuzhangli@ucla.edu

This PDF file includes:

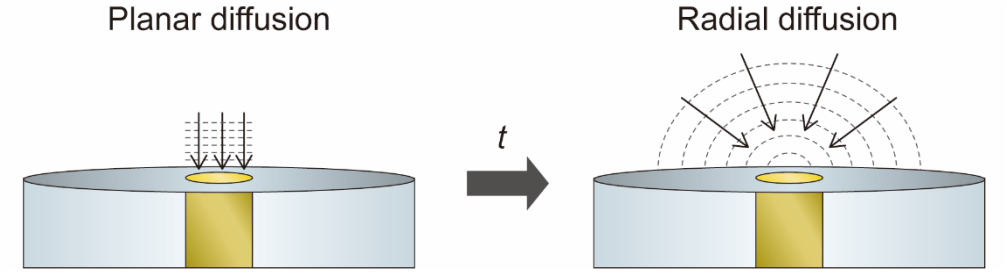
Supplementary Figs. 1 to 12



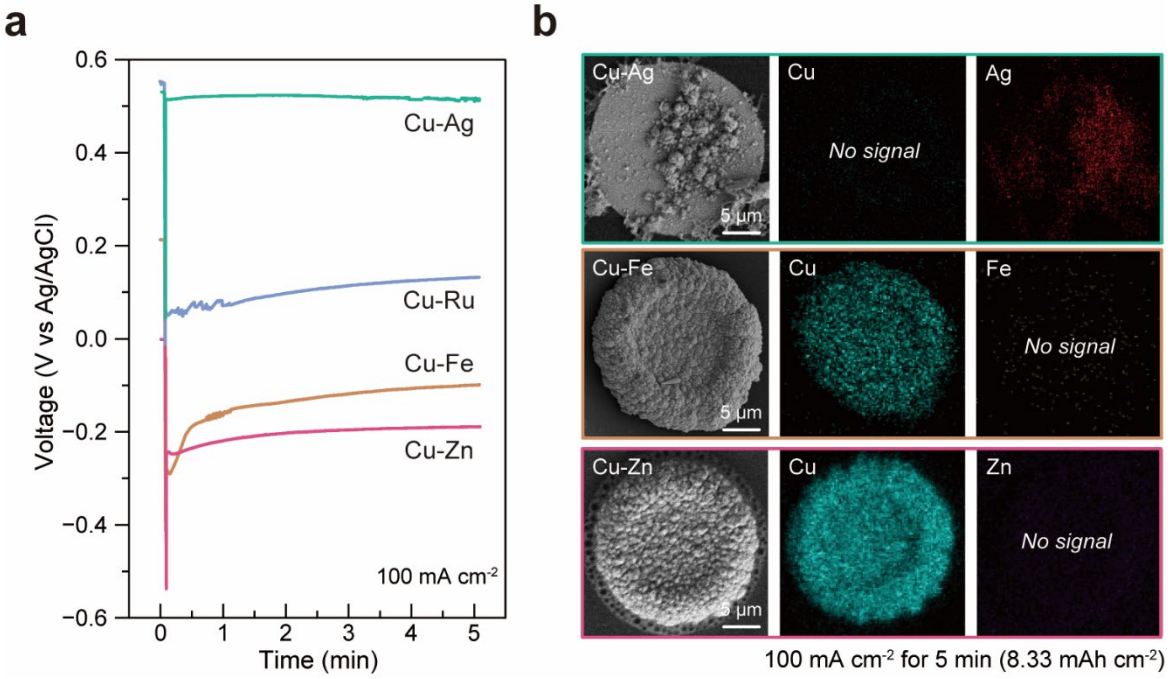
Supplementary Fig. 1. Fabrication and electrochemical characteristics of the customized ultramicroelectrode. a, Schematic illustration of the fabrication procedure for the glass-encapsulated metal-wire UME, including flame-assisted glass pulling, sealing of the metal wire, epoxy filling, and electrical connection. A photograph of the fabricated electrode is shown on the right. **b**. Photograph and optical microscopy images of the customized UME containing a 25-µm-diameter tungsten wire and the exposed electrochemically active area at the electrode tip. **c**. Schematic illustration of electrochemical mass transport at a UME. The small electrode dimensions enable high current densities at low absolute current, reduced ohmic loss and double-layer charging, and time-resolved access to the transition from early-time planar to radial diffusion.



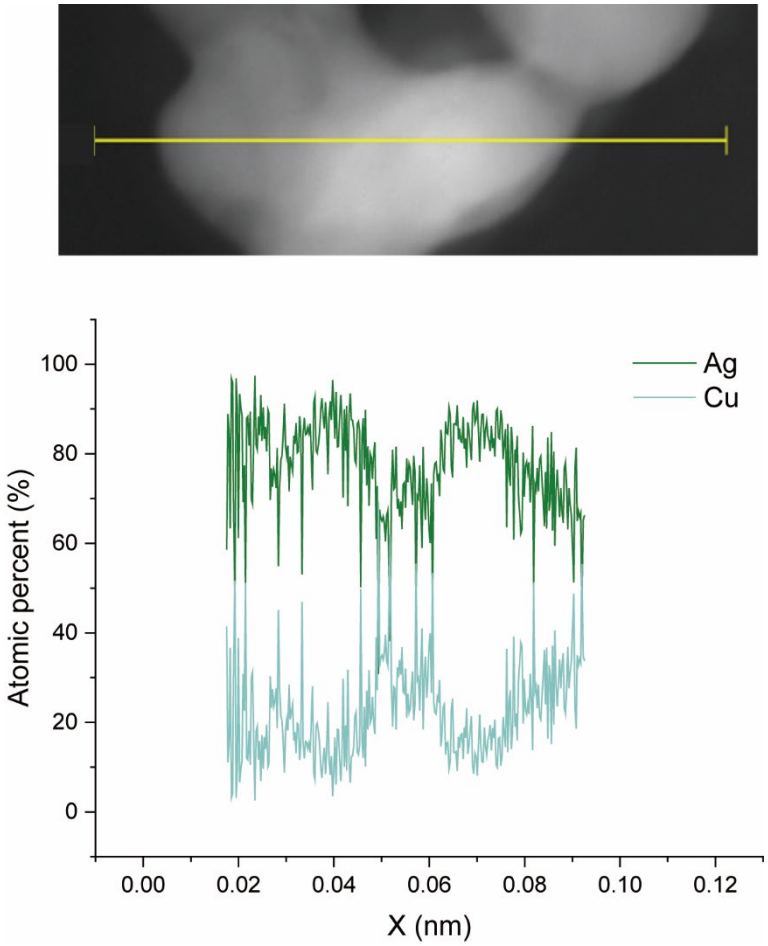
Supplementary Fig. 2. Galvanostatic voltage response of the Cu–Ag system over a wide range of current densities. a, Voltage–time profiles obtained during Cu–Ag deposition at 10^2, 10^3, 10^4, and 10^5 mA cm^{-2}. The inset magnifies the quasi-steady-state region and compares the Cu–Ag electrolyte with corresponding Cu-only measurements at identical current densities, illustrating the contribution of Ag^+ reduction to the steady-state potential. **b**, Enlarged view of the first 2 s after current application, highlighting the current-density-dependent transient polarization preceding establishment of the quasi-steady-state regime.



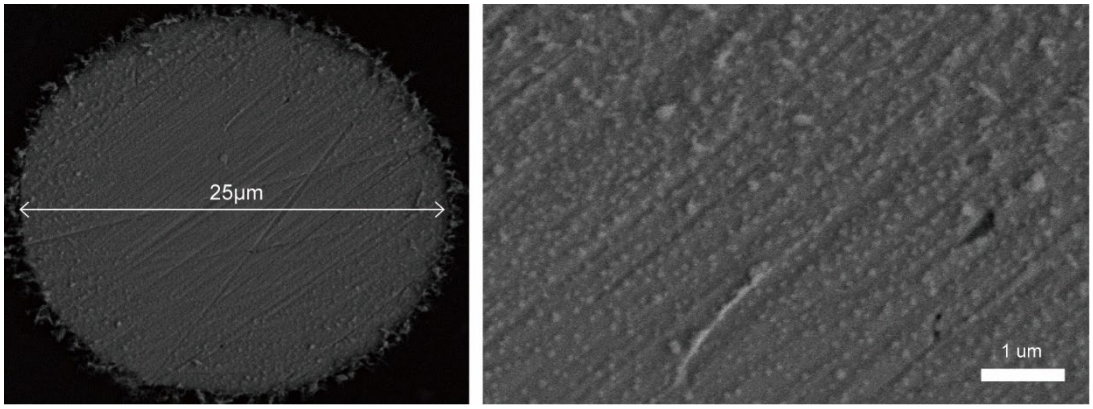
Supplementary Fig. 3. Evolution from planar to radial diffusion at an ultramicroelectrode. Schematic illustration of the time-dependent diffusion field at a disk UME. Immediately after electrochemical perturbation, the diffusion-layer thickness is small relative to the electrode radius and transport is predominantly planar. As the diffusion layer expands with time, edge effects become increasingly important and the concentration field evolves toward hemispherical radial diffusion, enabling continuous replenishment of electroactive species from the bulk electrolyte.



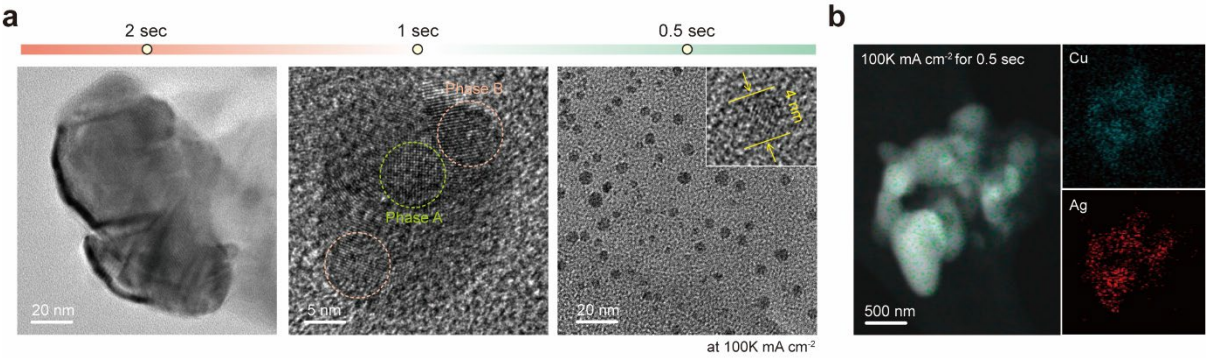
Supplementary Fig. 4. Electrochemical selectivity during conventional low-current deposition of binary metal-ion systems. a, Galvanostatic voltage–time responses of Cu–Ag, Cu–Ru, Cu–Fe, and Cu–Zn electrolytes during deposition at 100 mA cm^{-2}. **b**, SEM images and corresponding elemental maps of Cu–Ag, Cu–Fe, and Cu–Zn deposits obtained at 100 mA cm^{-2} for 5 min (8.33 mAh cm^{-2}). Ag is selectively deposited in the Cu–Ag system, whereas Cu dominates the Cu–Fe and Cu–Zn deposits, demonstrating reduction-potential-driven elemental selectivity under prolonged low-current conditions.



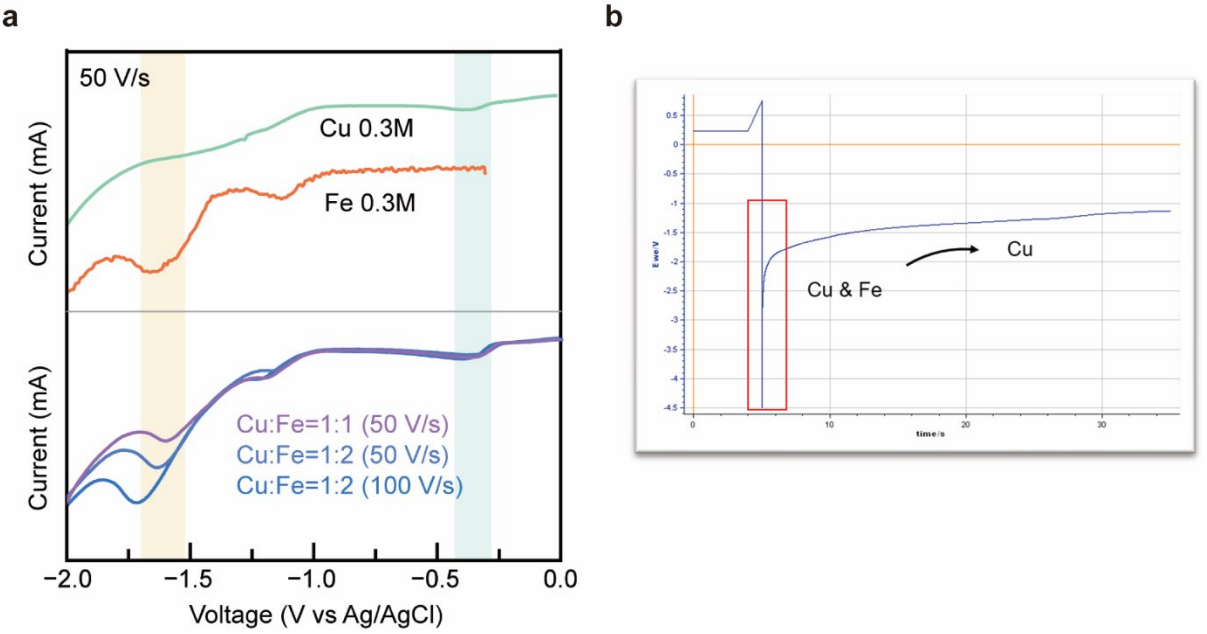
Supplementary Fig. 5. Spatial compositional heterogeneity of Cu–Ag formed under continuous deposition. Representative STEM image of a Cu–Ag deposit and corresponding EDS line profile acquired along the indicated trajectory. Spatial variations in the Cu and Ag atomic fractions reveal compositional heterogeneity and Ag-rich regions, demonstrating that partial Cu incorporation under continuous deposition does not necessarily produce homogeneous elemental mixing.



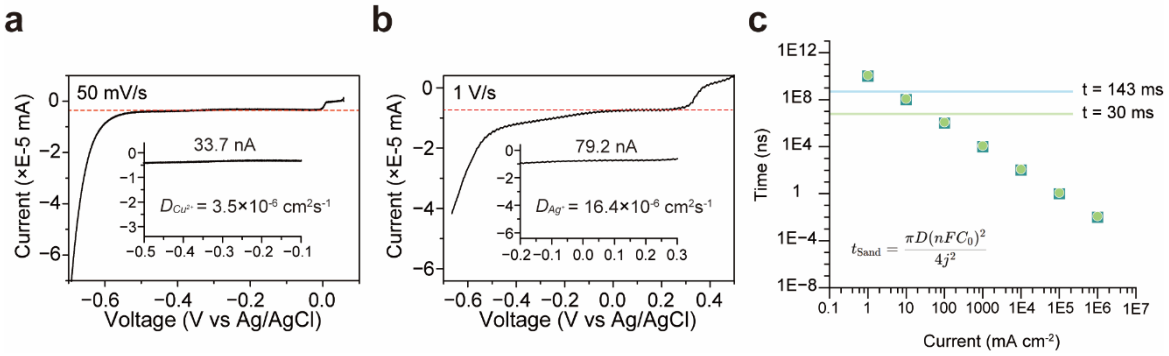
Supplementary Fig. 6. Morphology of Cu–Ag deposits formed under ultrahigh-current conditions. Low- and high-magnification scanning electron microscopic images of the 25 μm UME surface after ultrahigh-current Cu–Ag deposition. The higher-magnification image shows the fine-scale particulate morphology generated on the electrode surface under the strongly transient deposition conditions.



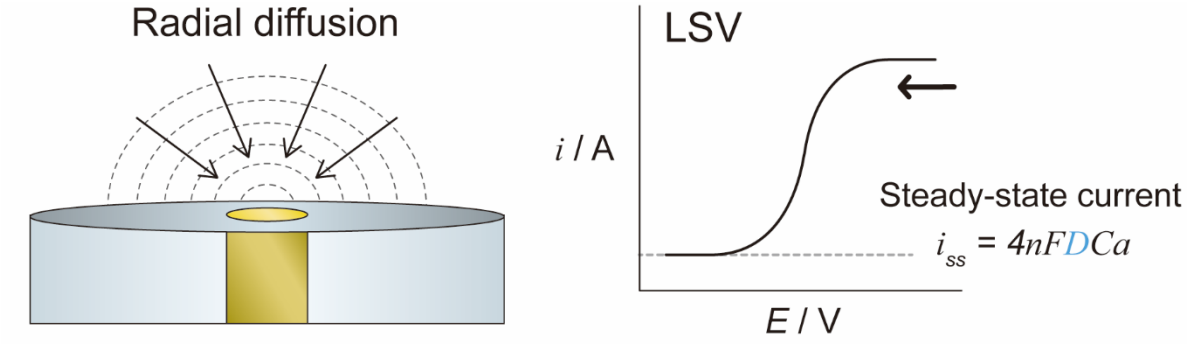
Supplementary Fig. 7. Pulse-duration-dependent morphology and composition of Cu–Ag deposits at ultrahigh current density. a, TEM and high-resolution TEM images of Cu–Ag deposits obtained with progressively shorter deposition durations of 2, 1, and 0.5 s at 100,000 mA cm^{-2}. Shortening the deposition time progressively suppresses particle growth, with nanoscale deposits obtained at the shortest duration; distinguishable crystalline domains are visible at intermediate deposition time. **b**, STEM image and corresponding Cu and Ag elemental maps of deposits obtained at 100,000 mA cm^{-2} for 0.5 s, showing incorporation of both elements within the pulse-generated nanostructures.



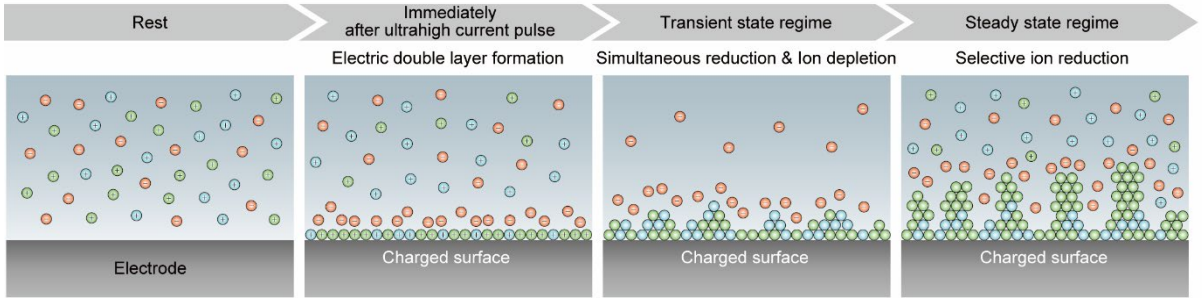
Supplementary Fig. 8. Electrochemical origin of transient-to-steady-state compositional evolution in the Cu–Fe system. a, Linear sweep voltammograms of Cu- and Fe-containing electrolytes, including individual 0.3 M Cu and Fe solutions and mixed Cu:Fe electrolytes with different concentration ratios and scan rates. The measurements identify the potential regions associated with Cu and Fe reduction and their overlap under strongly cathodic polarization. **b**, Representative potential transient during Cu–Fe deposition. The strongly negative early-time potential provides access to reduction of both Cu and Fe, whereas relaxation toward the steady-state potential progressively favors Cu deposition, providing an electrochemical basis for the transient-to-steady-state elemental segregation observed in Fig. 2f



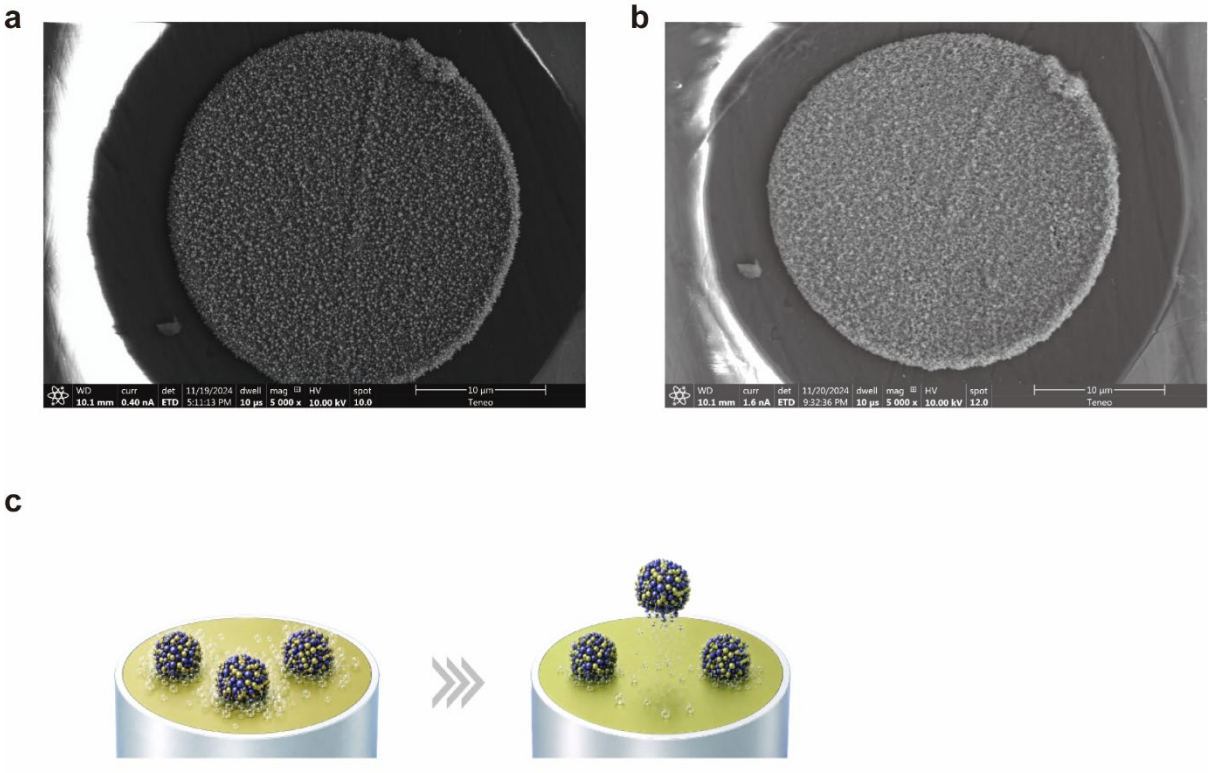
Supplementary Fig. 9. Electrochemical determination of ionic diffusivity and calculation of Sand's time. a, Linear sweep voltammogram used to determine the steady-state limiting current of Cu^{2+} at the UME. A limiting current of 33.7 nA gives a Cu^{2+} diffusivity of 3.5×10^{-6} $cm^2\ s^{-1}$. **b**. Corresponding measurement for Ag^+, yielding a limiting current of 79.2 nA and a diffusivity of 1.64×10^{-5} $cm^2\ s^{-1}$. **c**, Calculated Sand's time as a function of applied current density. The rapid decrease in Sand's time with increasing current density is compared with the characteristic radial-diffusion timescales, including the ~30 ms timescale associated with Ag^+ replenishment used to define the upper boundary of the Cu–Ag transient co-reduction window.



Supplementary Fig. 10. Determination of ionic diffusivity from the steady-state current at an ultramicroelectrode.
Schematic illustration of radial diffusion to a disk UME and the corresponding steady-state response during linear sweep voltammetry. Under radial diffusion, the steady-state limiting current is related to the ionic diffusivity through $i_{ss}=4nFDCa$, where n is the number of transferred electrons, F is the Faraday constant, D is the ionic diffusivity, C is the bulk concentration, and a is the electrode radius.



Supplementary Fig. 11. Temporal evolution of the interfacial reaction environment during ultrahigh-current deposition. Schematic sequence illustrating the transition from the resting state to transient and steady-state electrochemistry following application of an ultrahigh-current pulse. Immediately after current application, charging of the electrical double layer and rapid ion consumption establish a strongly polarized interface. During the transient regime, depletion of the preferentially reduced species enables simultaneous reduction of dissimilar ions. At longer times, bulk-ion replenishment restores electrochemical selectivity and the reaction evolves toward preferential deposition of the more readily reduced species.



Supplementary Fig. 12. Hydrogen-evolution-induced detachment of unsupported electrodeposited particles. a,b, Representative SEM images of an unsupported particle-covered electrode before and after gas-evolving electrochemical operation, respectively, illustrating changes in surface coverage associated with particle detachment. **c**, Schematic illustration of bubble-induced removal of weakly adhered alloy particles from the electrode surface during hydrogen evolution